Space-based Femtosecond Laser Filamentation

Final Report

Authors: V. Jukna[1], A. Couairon[1], I. Dicaire[2], C. Praz[2], C. Milian[1], L. Summerer[2]
Affiliation: [1]École Polytechnique, [2]Advanced Concepts Team, ESA

Date: 15/01/2015

Contacts:

Arnaud Couairon
Tel: +33(0)16 933 4224
Fax: +33(0)16 933 4949
e-mail: Arnaud.Couairon@cpht.polytechnique.fr

Leopold Summerer (Technical Officer)
Tel: +31(0)71 565 4192
Fax: +31(0)71 565 8018
e-mail: act@esa.int

Available on the ACT website
http://www.esa.int/act

Ariadna ID: 13-9201
Ariadna study type: Standard
Contract Number: 4000111104/14/NL/MV

Ariadna 4000111104/14/NL/MV: Space-based Femtosecond Laser Filamentation [13-9201]

V. Jukna[1], A. Couairon[1], I. Dicaire[2], C. Praz[2], C. Milian[1], L. Summerer[2]

[1]Centre de Physique Théorique, École Polytechnique, CNRS, F-91128, Palaiseau, France
vytautas.jukna@cpht.polytechnique.fr,arnaud.couairon@cpht.polytechnique.fr,carles.milian@cpht.polytechnique.fr
[2]Advanced Concepts Team, European Space Agency, Keplerlaan 1, P.O. Box 299, NL-2200AG Noordwijk, the Netherlands
isabelle.dicaire@esa.int;christophe.praz@esa.int;leopold.summerer@esa.int

Contents

Chapter 1

INTRODUCTION

Remote sensing of the atmosphere via Earth-orbiting satellites provide essential information in the field of climate science and atmospheric chemistry. Driven by the need to improve our understanding of climate change, remote sensing instrumentation aims at providing high resolution measurements of key trace constituents on a global scale with high accuracy [1]. Monitoring of long-lived greenhouse gases such as carbon dioxide and methane is required at adequate spatial and temporal sampling to disentangle anthropogenic from natural sources. Monitoring of short-lived pollutants such as volatile organic compounds and radiatively active gases such as tropospheric ozone and nitrogen oxides is also required because of their impact on human health and climate change [2–5]. Furthermore ozone molecules play a critical role in atmospheric chemistry; they are involved in chemical reactions producing the hydroxyl radical, which provides a natural self-cleansing mechanism to eliminate atmospheric pollutants [6]. Ozone chemistry is a complex phenomena which needs to be better understood in view of global warming, ozone loss, and tropospheric pollution [1, 5, 7, 8]. To help answer these questions multispectral synoptic observations of key atmospheric trace constituents at different atmospheric depths are required at sufficient spectral and spatial resolution with adequate accuracy [9, 10].

Over the past years, a variety of spaceborne instruments such as imaging spectrometers have been developed to improve our understanding of ozone chemistry and climate change [11–16]. However such spectrometers are limited to column-integrated amounts along the line of sight in the nadir and sun glint modes [11]. Vertical profiles can be retrieved for the stratosphere in the solar occultation mode but they typically suffer from large uncertainties and low vertical resolution [17–19]. In addition spaceborne spectrometers poorly cover critical source regions such as the Arctic circle and Boreal forests and cannot investigate day-night cycles. On the other hand, active lidar instruments such as differential absorption lidars offer a better retrieval of greenhouse gas fluxes with greater accuracy and they avoid potential biases due to atmospheric column amounts by providing precise vertical information of greenhouse gas concentrations [20]. They can also provide measurements in dark polar regions to better constrain natural greenhouse gas sources. In addition vertical profiles of clouds and aerosols can be obtained by measuring backscattering coefficients but require *a priori* estimations to calculate aerosol size distributions. Finally current spaceborne lidar technology is limited in target gas species and their

corresponding laser wavelengths.

To address such shortcomings, spaceborne remote sensing instrumentation could benefit from current advances in the field of laser filamentation and ground-based white-light lidar technology. Laser filamentation, resulting from the nonlinear propagation of intense ultrashort laser pulses in the atmosphere, has become a promising tool in the field of remote sensing of pollutants and bioaerosols. In this technique, powerful femtosecond laser pulses propagate in the atmosphere and can deliver high intensities at altitudes reaching 20 km from the ground. High intensities lead to a competition between various physical effects including the optical Kerr effect focusing the beam and laser energy absorption, which in turn leads to plasma generation and plasma-induced beam defocusing. This competition results in the formation of thin filaments where efficient nonlinear phenomena can be sustained over several tens of meters, among which self-phase modulation leads to the generation of a coherent broadband continuum spanning from ultraviolet to near infrared wavelengths [21]. Filamentation at kilometric distances with ultrashort optical pulses has been demonstrated for vertical propagation from ground to sky [22, 23] and for horizontal propagation [24–26] and white-light lidar measurements have been performed using a single laser source [27–29]. On the other hand, theoretical and numerical investigations of pulse propagation leading to filamentation have been mostly restricted to the regime of laboratory filaments [30] and short scale outdoor filaments [24]. The few theoretical studies on long distance pulse propagation made assumptions and approximations that are no longer valid for a 400-km study, e.g. a constant atmospheric density profile as in [31–33].

It is now well understood that the optical Kerr effect is one of the most important effects in laser filamentation. In order to form a filament, a pulse power P exceeding a critical threshold ($P_{cr} \sim 3$ GW in air at ground level) is required. Before forming a filament, the beam undergoes a self-focusing stage over a distance proportional to the diffraction length $z_R = \pi w_0^2/\lambda_0^2$, where w_0 denotes the $1/e^2$ input beam width and λ_0 the laser wavelength, and to the expression $(P/P_{\mathrm{cr}}-1)^{-1/2}$. Thus, large beams will form filaments at long distances whereas increasing the pulse power shortens the self-focusing stage. Actually all observations of high intensities and filament signatures at large distances resulted from a control of the prefilamentation (self-focusing) stage by chirping the laser pulse, resulting in a longer pulse with lower initial peak power, effectively delaying the filament formation up to the required propagation distance or altitude. If the chirp is negative, the pulse is recompressed while it propagates due to the effect of group velocity dispersion, and reaches the end of the prefilamentation stage with high power. From laboratory and outdoor experiments [34–36], filamentation is known to occur at low pressure, i.e., low gas density. However if the gas density decreases below a certain threshold, the critical power increases above the pulse power, making self-focusing and filamentation impossible. Finally white-light lidar applications (i.e. with femtosecond laser pulses) are difficult to investigate and realise due to the limited control over the pulse propagation to the altitude of interest; efficient supercontinuum generation over the wavelength range required for a particular application is therefore not guaranteed.

In spite of these issues, spaceborne laser filamentation might offer attractive applications for atmospheric science. For instance it offers simultaneous range-resolved measurements of key atmospheric trace gas constituents including ozone, nitrogen oxides, bromine oxide, volatile organic compounds, water

vapour, carbon dioxide, and methane via absorption bands ranging from the ultraviolet to the near infrared (300nm–3μm). In addition synergistic retrievals of atmospheric pressure and temperature information would be possible via high spectral resolution observations of oxygen (O_2) lines. Currently such information is obtained via collocated data from weather forecasting models but direct retrievals from oxygen spectral lines is sought in the future [17]. The coherent broadband light continuum generated by the filamentation process is also very attractive for aerosol and cloud characterisation. It could in particular enable direct measurements of relative humidity profile from synergistic observations of oxygen and water vapour lines to improve our understanding of cloud formation and precipitation [37]. It could also lead to a better retrieval of water droplet and aerosol size distribution and density from multiwavelength backscattering coefficients without providing *a priori* knowledge of the cloud or aerosol properties [37]. Finally filaments in air seem to survive propagation through rain or fog; this apparent robustness is due to the self-healing property of filaments. The surrounding, lower intensity section of the filament establishes an energy flux towards the intense filament core whenever it undergoes losses due to the presence of an obstacle or a strong absorber, playing the role of an energy reservoir. Such property could extend the use of optical wavelengths applications over a broader range of meteorological conditions. In addition, other applications could benefit from the possibility to control the generation of spaceborne laser filaments. For instance, wireless power transportation from space to Earth and directed energy applications based on self-focusing in the atmosphere have been proposed [32].

In this paper, we present theoretical and numerical investigations of nonlinear optical pulse propagation from a 400-km altitude towards the ground. The structure of the paper is the following. Chapter 2 presents the full numerical model for the simulation of filamentation including the optical Kerr effect, diffraction laws, plasma defocusing, and multiphoton absorption in the presence of various ionizing species varying with altitude. Chapter 3 presents the theoretical analysis of self-focusing with state-of-the-art models and presents new scaling laws for the collapse distance in the presence of a stratified atmosphere. Chapter 4 presents the results of the direct numerical simulations of filamentation from orbit including a detailed analysis of the beam width and pulse intensity dependence on height. Results on the supercontinuum generated at the collapse point (i.e. at 7.3 km from ground) and beyond are also presented in this chapter. Chapters 5 and 6 conclude with summarizing statements and options for future works. Finally the full description of the theoretical model developed for the vertical propagation of ultrashort laser pulses can be found in Appendix A.

Chapter 2

Model for numerical simulations of filamentation from orbit

2.1 Model Description

Our numerical simulations are based on a unidirectional propagation equation along the direction z for the spectral components $\hat{\tilde{E}}(\omega, k_x, k_y, z)$ of the electric field envelope $\mathcal{E}(t, x, y, z)$ of the laser pulse [38]

$$\partial_z \hat{\tilde{\mathcal{E}}} = i[\sqrt{k^2(\omega) - k_\perp^2} - k_0 - k_0'(\omega - \omega_0)]\hat{\mathcal{E}} + i\frac{\mu_0}{2k(\omega)}(\omega^2 \hat{\tilde{\mathcal{P}}} + i\omega \hat{\tilde{\mathcal{J}}}), \qquad (2.1)$$

where a hat denotes Fourier transform from time to frequency, a tilde denotes Fourier transform from space to wavenumbers and $k_\perp^2 \equiv k_x^2 + k_y^2$. Hence $\hat{\tilde{P}}(\omega, k_x, k_y, z)$ and $\hat{\tilde{J}}(\omega, k_x, k_y, z)$ denote the Fourier components for the nonlinear polarization and current sources, describing the medium response. The quantities $k(\omega) \equiv n(\omega)\omega/c$ denotes the dispersion relation of air [39] whereas $k_0 \equiv k(\omega_0)$ and $k_0' \equiv dk/d\omega|_{\omega_0}$ are taken at the central frequency ω_0 of the laser.

We will also consider the monochromatic version of Eq. (2.1)

$$\partial_z \tilde{\mathcal{E}} = i[\sqrt{k_0^2 - k_\perp^2} - k_0]\tilde{\mathcal{E}} + i\frac{\mu_0}{2k_0}(\omega_0^2 \tilde{\mathcal{P}} + i\omega_0 \tilde{\mathcal{J}}), \qquad (2.2)$$

where $\tilde{\mathcal{E}}(k_x, k_y, z)$, as well as $\tilde{\mathcal{P}}(k_x, k_y, z)$ and $\tilde{\mathcal{J}}(k_x, k_y, z)$ no longer depend on the frequency ω.

The response of the medium is described by the laws which link the nonlinear polarization $\mathcal{P}(t, x, y, z)$ and the current $\mathcal{J}(t, x, y, z)$ to the electric field envelope. Our model accounts for the optical Kerr effect, ionization and plasma effects including nonlinear absorption of energy and plasma defocusing. These

phenomena are described by the set of equations

$$\mathcal{P} = 2\epsilon_0 n_0 n_2 \mathcal{I}\mathcal{E}, \tag{2.3}$$

$$\mathcal{J} = \epsilon_0 n_0 c \sum_s (\sigma_s \rho_e + \beta_{K_s} \mathcal{I}^{K_s - 1})(1 - \frac{\rho_{s^+}}{\rho_{s,b}})\mathcal{E} + i\epsilon_0 \omega_0 \frac{\rho_e}{\rho_{cr}} \mathcal{E} \tag{2.4}$$

$$\frac{\partial \rho_{s^+}}{\partial t} = (\sigma_{K_s} \mathcal{I}^{K_s} \rho_{s,b} + \frac{\sigma_s \mathcal{I}}{U_{i,s}} \rho_e)(1 - \frac{\rho_{s^+}}{\rho_{s,b}}) \tag{2.5}$$

$$\rho_{s^+} = \rho_{s,b}(z) - \rho_s \tag{2.6}$$

$$\rho_e = \sum_s \rho_{s^+} \tag{2.7}$$

The quantity $\mathcal{I} \equiv \epsilon_0 n_0 c|\mathcal{E}|^2/2$ denotes the pulse intensity and n_2 denotes the nonlinear index coefficient. The quantities $\rho_s(t,x,y,z)$, $\rho_{s^+}(t,x,y,z)$ and $\rho_e(t,x,y,z)$ denote the density of neutral atomic or molecular species s (nitrogen N_2, oxygen O_2, etc), ions s^+ generated by single ionization and electrons, respectively. The density $\rho_{cr} \equiv \epsilon_0 m_e \omega_0^2/e^2$ denotes the critical plasma density beyond which the plasma becomes opaque to the wave of frequency ω_0. The quantity $K_s \equiv \langle \frac{U_{i,s}}{\hbar\omega_0} + 1 \rangle$, where brackets mean the integer part, denotes the number of photons necessary for an atom or molecule with ionization potential $U_{i,s}$ to liberate an electron by multiphoton ionization, with rate coefficient σ_{K_s}. The corresponding multiphoton absorption coefficient $\beta_{K_s}(z) \equiv \sigma_{K_s} K_s \hbar\omega_0 \rho_{s,b}(z)$ and the plasma absorption cross section $\sigma_s(z) \equiv (\tau_s(z) n_0 c \rho_{cr})^{-1}$ are both proportional to the background density of s species $\rho_{s,b}(z)$ before the passage of the pulse. The parameters n_2, β_{K_s}, σ_s and the collision time $\tau_{c,s}$ thus all depend on altitude whereas other parameters ($U_{i,s}$, K_s, σ_{K_s}, ρ_{cr}) are constant. Reference values for the parameters are given in table 2.1.

(a) Parameters for air at ground level

Parameter	Value
λ_0 [nm]	800
n_0	1.
$n_{2,0}$ [cm^2/W]	3×10^{-19}
$\rho_{\mathrm{air},0}$ [cm^{-3}]	2.5×10^{19}

(b) Material Parameters for each species

Species s	O_2	N_2	Ar
$\rho_{s,0}$ [cm^{-3}]	5.25×10^{18}	1.96×10^{19}	2.33×10^{17}
$U_{i,s}$ [eV]	12.063	15.576	15.759
K_s	8	11	11
$\sigma_{K_s,s}$ [$\mathrm{s}^{-1}\mathrm{cm}^{2K_s}\mathrm{W}^{-K_s}$]	3.6×10^{-96}	7.5×10^{-140}	6.0×10^{-140}
$\beta_{K_s,s,0}$ [$\mathrm{cm}^{2K_s-3}\mathrm{W}^{-K_s+1}$]	1.8×10^{-94}	5.1×10^{-138}	4.1×10^{-138}
$\tau_{c,s,0}$ [fs]	350	350	190
$\sigma_{s,0}$ [cm^2]	5.47×10^{-20}	5.47×10^{-20}	1.01×10^{-19}

Table 2.1: Material parameters.

In Appendix A, we show that the model derived for vertical propagation of

ultrashort laser pulses from orbit to ground therefore consists in a formally similar propagation equation (2.1) (or (2.2)) and medium response model Eqs.(2.3)–(2.7) as those used at sea level. However, some coefficients in the model vary with the density of species (oxygen, nitrogen, etc) in air and therefore will depend on the density distribution across the atmosphere.

We define a species-dependent density profile function $F_s(z)$

$$F_s(z) \equiv \frac{\rho_{\mathrm{s,b}}(z)}{\rho_{\mathrm{air},0}}, \tag{2.8}$$

where $\rho_{air}(z) = \sum_s \rho_{s,b}(z)$ and $\rho_{\mathrm{air},0}$ denotes a reference value for the density of air at sea level $z = 0$.

The corresponding variation of model parameters is then as follows:

$$n_2(z) = n_{2,0} \times F_{\mathrm{air}}(z), \tag{2.9}$$

$$\beta_{K,s}(z) = \beta_{K,s,0} \times F_s(z), \tag{2.10}$$

$$\sigma_s(z) = \sigma_{s,0} \times F_s(z), \tag{2.11}$$

$$\tau_{c,s}^{-1}(z) = \tau_{c,s,0}^{-1} \times F_s(z), \tag{2.12}$$

where $\sigma_{s,0} \equiv (n_0 c \rho_{cr} \tau_{s,0})^{-1}$. The dependency of coefficients upon altitude is fully determined by the dependence of air and molecular or atomic species densities upon altitude as indicated in Eqs (2.9) to (2.12). Other coefficients such as ionization potentials and cross sections for multiphoton ionization $\sigma_{8,(O_2)}$, $\sigma_{11,(N_2)}$ do not depend on species density. These expressions show that the nonlinear dynamics is not expected to be trivially rescaled with air pressure or density, since the density of different species enters in different physical effects (plasma induced defocusing, plasma absorption terms) with a different scaling. Therefore, the numerical investigation is important in order to reveal the changes in the competition between the nonlinear effects when the density of species varies with altitude.

2.2 Atmospheric Data Sources

As mentionned above, the medium response to the laser beam propagation depends on the gas species density. The atmospheric density profiles used to run our simulation come from NRLMSISE-00, the latest update of the MSIS-class model, which is the standard for international space research. NRLMSISE-00 is an empirical and global model of the Earth's atmosphere from ground to thermospheric heights and is freely available on the Community Coordinated Modeling Center (CCMC) online platform [40]. The initial model database derived from ground-, rockets- and satellite-based measurements has been extended on two occasions to include incoherent scatter radar and mass spectrometer data (1990) as well as drag on satellites and other space objects (2001)[40]. Under 72.5 km, the model is primarily based on the Middle Atmosphere Program (MAP) Handbook [41] giving tabulated values for zonal average temperature and pressure, supplemented with data from the National Meteorological Center below 20 km.

Giving the geographic coordinates, the date and the time of the day, the model calculates vertical profiles of neutral temperature, densities of He, O, O_2, N, N_2, Ar, H as well as total air mass density.

The model provides excellent average values for each atmospheric layer from 400-km altitude to ground level; it is thus well suited for the current study, which aimed at modelizing laser filamentation from orbit under typical atmospheric conditions. The species density profiles implemented in the medium's response model are shown in Fig. 2.1. They correspond to values averaged over several day and night records taken during Spring 2014 above Western Europe.

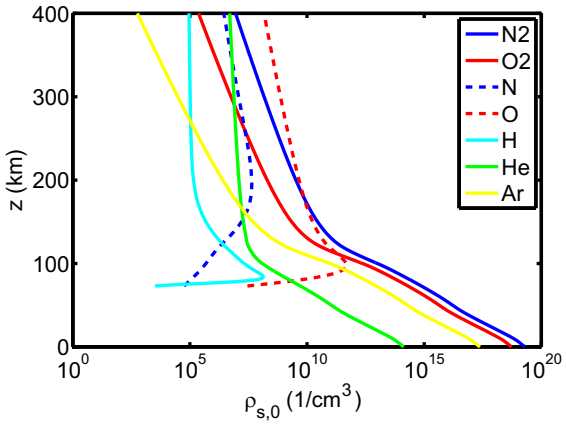

Figure 2.1: Species density dependence on height retrieved via MSIS-class model.

From Fig. 2.1, the dominant species to be considered in the model are molecular nitrogen and oxygen between sea level and 120 km. Contributions to the generated plasma of species with neutral densities that are orders of magnitude below the density of the dominant species will be negligible. This is verified in Fig. 4.5 where the optical field and avalanche ionization by a 500-fs pulse with peak intensities typically found in filaments are considered for all species depicted in Fig. 2.1.

Chapter 3

Theoretical analysis of self-focusing from orbit

3.1 Theoretical formulation

At sea level, a filament is usually generated after an initial self-focusing stage, which requires the beam power to be above a critical threshold. During this stage, the beam diameter shrinks from its initial value to the filament width. This occurs because the beam intensity is higher in the center of the beam, which therefore feels a higher refractive index due to the optical Kerr effect. Similarly to the effect of a focusing lens, this leads to phase curvature accumulation and beam focusing, except that the effect is cumulative and may in principle lead to beam collapse, at finite distance on axis. However the beam intensity just before collapse is sufficiently high so that nonlinear absorption phenomena starts setting in, preventing a catastrophic collapse of the beam and leading to the formation of a filament. An optical beam launched from orbit towards the ground will form a filament in the atmosphere provided the optical power is high enough and the beam collapse location is reached before the ground. In order to determine the conditions that laser parameters must satisfy for filament formation, we first extended the state-of-the-art theory for beam self-focusing and collapse to the case of a stratified atmosphere (see Appendix A), based on the paraxial version of Eq. (2.2), when diffraction and the optical Kerr effect are the only effects included in the model.

Scaling laws for the collapse distance are obtained by introducing Eq. (2.3), $\mathcal{J} = 0$ and a small $k_\perp/k_0$-expansion into Eq. (2.2), which is rewritten here in the space-time domain for the electric field envelope $\mathcal{E}(x, y, z)$

$$\frac{\partial \mathcal{E}}{\partial z} = \frac{i}{2k_0}\nabla_\perp^2 \mathcal{E} + i\frac{\omega_0}{c} n_2 |\mathcal{E}|^2 \mathcal{E} \tag{3.1}$$

For a constant n_2, a scaling law for the position of collapse is readily obtained analytically from Eq. (A.12) by means of the moment theory [30, 42, 43], which consists in deriving for a Gaussian beam

$$\mathcal{E}(r, z) = \left(\frac{P(z)}{\pi R^2(z)}\right)^{1/2} \exp\left(-\frac{r^2}{2R^2}\right) \times \exp\left[ik_0 \frac{R'(z) r^2}{2R(z)} + i\phi_0(z)\right], \tag{3.2}$$

where $r^2 \equiv x^2 + y^2$, the ordinary differential equation governing the evolution of the beam radius $R^2(z) \equiv P^{-1}(z) \int r^2 |\mathcal{E}|^2 d\mathbf{r}$ along z

$$\frac{d^2R}{dz^2} = \frac{1}{k_0^2 R^3} \left(1 - \frac{P}{P_{cr}^*}\right), \tag{3.3}$$

where P is the preserved beam power and $P_{cr}^* \equiv \lambda_0^2 / 2\pi n_0 n_2$. Provided the critical power P_{cr}^* is constant, Eq. (A.14) admits the solution $R^2(z) = R_0^2 \left[(1 + (R_0'/R_0)z)^2 - z^2/z_c^2\right]$ where $z_c \equiv k_0 R_0^2 / \sqrt{P/P_{cr}^* - 1}$ denotes the collapse distance without initial focusing. R_0 denotes the initial beam width and R_0' is negative when the beam is focused by a lens. In the latter case, the beam radius vanishes at $z_{c,f}$ given by $z_{c,f}^{-1} = z_c^{-1} + f^{-1}$ where $f = -R_0/R_0'$.

3.2 Beam self-focusing and collapse in a stratified atmosphere

In a stratified atmosphere, Eq. (3.1) remains valid provided the single parameter, the nonlinear index coefficient n_2, varies with altitude. The only assumption in the derivation of Equation (3.3) from Eq. (3.1) is that n_2 does not depend on the transverse coordinates x and y, but the same equation remain valid if n_2, and thus P_{cr}^* vary with altitude z. However the above analytical solution to Eq. (3.3) no longer holds. Equation (3.3) can only be integrated numerically in the case of a z-dependence of P_{cr}^*.

Figure 3.1 shows a comparison between the collapse distance obtained by numerical integration of Eq. (3.3) and by direct numerical simulation of Eq. (3.1). The input conditions correspond to a Gaussian beam launched from orbit, i.e., $z_0 = 400$ km, $R_0 = 50$ cm, $\lambda_0 = 800$ nm, $R_0' = R_0/f$ with $f = 390$ km (note the sign of the beam curvature is positive when focusing from orbit to ground), and the input power P is varied from 1 to 1000 $P_{cr,0}^*$ (3 GW to 3 TW). The trend is similar for both methods, i.e. the position of the collapse and therefore the beginning of the filament is closer to the launching orbit when the beam power is higher. However, at any given input power, a significant difference is obtained for the collapse distances calculated by the two methods. This is due to the fact that the semi-analytical method leading to the derivation of Eq. (3.3) assumes that the beam stays Gaussian, while the direct numerical simulation of Eq. (3.1) allows for beam reshaping during self-focusing. Although the collapsing beam shape still looks Gaussian, a final difference of several kilometers is obtained in the positions of the collapse distance after a propagation over 400 km in the stratified atmosphere.

3.3 Scaling laws for the collapse distance in a stratified atmosphere

By numerically integrating Eq. (3.1) with a nonlinear refractive index dependence on altitude, we performed a parametric study of the collapse distance dependence upon the beam diameter and power. We used here the atmospheric data sources presented in Fig. 2.1 to retrieve the density profile of air and the

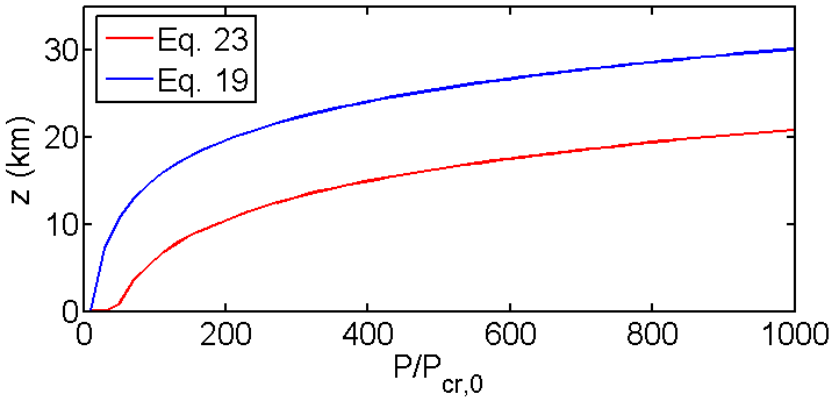

Figure 3.1: Collapse distance dependence on initial beam power for two different approaches are depicted by different colors. The red curve shows the results obtained by numerical integration of Eq. (3.3), while the blue curve depicts the result of a direct numerical simulation of Eq. (3.1).

variation of nonlinear refractive index as a function of altitude. We again use the critical power for self-focusing at the ground level, $P^*_{cr,0}$, as a reference value for measuring input powers.

We first discuss the position of the beam collapse as a function of input beam power, for a fixed input beam radius $R_0 = 45$ cm at $z_0 = 400$ km and a fixed beam curvature $f = 390$ km, $R'_0 = R_0/f$. Figure 3.2a shows the evolution of beam radius from orbit to the altitude at which the beam collapses ($R(z) = 0$), or to the ground. Altitude is represented in log scale, hence, the values obtained at $z = 1$ km do not differ substantially from those on the ground. The continuous blue curve shows the case of linear propagation. The position of the linear focus is not located at $z_0 - f = 10$ km but at $z_f = z_0 - f/(1 + f^2/z_R^2)$, where $z_R = k_0 R_0^2$, i.e., at 32.121 km from the surface of Earth. This is due to the fact that the Rayleigh length z_R corresponding to the input beam is not significantly larger than the beam curvature f, thus the laws for Gaussian optics tell us that the focal distance substantially differs from the beam curvature radius. All other curves in Fig. 3.2a correspond to input powers that are higher than $P^*_{cr,0}$, i.e. these beams must collapse. Beams carrying larger power collapse at higher altitude as expected. The collapse position is found above ground only for beams with sufficiently high power (threshold between 10 and 60 $P^*_{cr,0}$). We note that all beams collapse beyond the linear focus (marked with a star), a situation seemingly incompatible with the lens law (Eq. (A.17)), but correct here as the latter is not valid for a stratified atmosphere. The propagation is actually quasi linear until the linear focus. Figure 3.2c shows when propagation enters in the nonlinear regime, i.e. when the curves intersect the vertical line $P/P^*_{cr}(z) = 1$. Nonlinear propagation is found to begin 15-45 km from the ground for power levels between 10 and 700 $P^*_{cr,0}$. Only beams carrying 300 and 700 $P^*_{cr,0}$ have entered the nonlinear regime before reaching the linear focus, but even in these conditions, the distance to collapse was larger than the distance to the linear focus.

Figure 3.2b shows the beam radius evolution for the same input conditions

except that the beam curvature was chosen so as to locate the linear focus exactly at 10 km from the ground ($z_f = 10$ km). According to the laws for Gaussian optics, the required beam curvature to satisfy this condition is $1/f = [1-(1-4d_f^2/z_R^2)^{1/2}]/2d_f$ with $d_f = z_0 - z_f = 390$ km, which yields $f = 6069$ km. We note that locating the linear focus at a predetermined position is only possible for sufficiently large beams satisfying $z_R = k_0 R_0^2 > 2d_f$. With $d_f = 390$ km, this means $R_0 > 31.5$ cm. The diffraction limit implies that a smaller beam simply cannot be focused linearly beyond a distance equal to half its Rayleigh length. In Figure 3.2b, the altitude of the linear focus (again marked with a star) is sufficiently far from the altitude at which the propagation becomes nonlinear ($P/P_{cr}^*(z) = 1$, see Fig. 3.2c).The beam radius thus clearly shrinks due to self-focusing before the beam reaches the linear focus.

Figures 3.2(d) and (e) show the beam radius evolution for a fixed power (700 $P_{cr,0}^*$) for different input beam radius and for a fixed beam curvature $f = 10$ km (the position of the linear focus depens on input beam width, Fig. 3.2d) or for a fixed position of the linear focus (the input beam curvature depens on input beam width, Fig. 3.2e). The curve $P/P_{cr}^*(z)$ in Fig. 3.2(f) should be read simultaneously as it indicates for which altitudes propagation is nonlinear ($z < 50$ km). At this altitude, all curves in Figs 3.2d and e start to depart from the superposed fine continuous curves representing the linear propagation of the same beams. These curves exhibit a minimum radius, marking the linear focus, the altitude of which depends on the input beam width. Only the smaller input beam $R_0 = 21$ cm cannot be focused linearly in the nonlinear region, and thus exhibits a defocusing stage before undergoing self-focusing. Since this beam cannot be fosused linearly at $z_f = 10$ km, the corresponding curve is absent in Fig 3.2e.

The results are summarized in Fig. 3.3 in the case of a fixed beam curvature $f = 390$ km. The white region corresponds to conditions for which collapse is not reached before the surface of Earth. For beams with parameters in this region, collapse would actually happen below the sea level. This happens even for beams carrying a power well above $P_{cr,0}^*$ because propagation is linear in the underdense upper layers of the atmosphere and the beam may be large or diverging when it enters in the nonlinear region (lower layers of the atmosphere), therefore requiring a self-focusing distance larger than the remaining propagation distance to the sea level. The two lines with various symbols in Fig.3.3a indicate slices of the parameter space shown in Fig.3.3b for the constant input beam width $R_0 = 45$ cm, and in Fig.3.3c for the constant power 700 $P_{cr,0}^*$. The collapse altitude gets larger (closer to the launching orbit) when the beam power increases for a constant input beam radius. For a fixed beam power, the collapse position shows a maximum altitude at a specific input beam radius. This is due to the fact that (i) very large beams correspond to large numerical apertures and tend to self-focus further from the linear focus, i.e., at higher altitudes when the input beam radius decreases. (ii) small beams cannot be focused linearly at $z = 10$ km but diverge the more they are initially smaller, after an initial short focusing stage. They eventually collapse further from the ground when the input beam radius increases.

From the numerical results presented in Fig. 3.3, we applied a trial and error procedure to obtain a scaling law that very closely match the collapse distance obtained by numerical simulations. The fit function reads

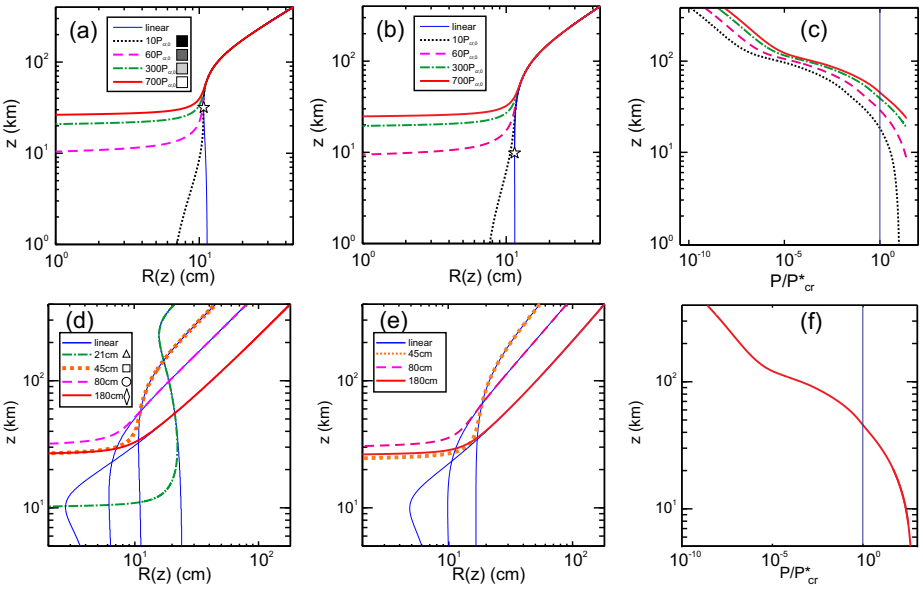

Figure 3.2: (a,b,d,e) Beam radius dependence on propagation distance. (c) and (f) Number of local critical powers $P/P_{cr}(z)$ carried by a beam of power P. In (a) and (b), the initial beam radius $R_0 = 45$ cm is constant, while beam power was changed from $10\,P{*}_{cr,0}$ to $700\,P{*}_{cr,0}$. The beam curvature is $f = 10$ km in (a) and (d) and $f = 6069$ km ($z_f = 10$ km) in (b) and (e). In (c) and (f), the vertical lines separate linear and nonlinear propagation regimes for the beam propagation shown on each row. In (d) and (e), the beam radius evolution is shown when the beam power was fixed at $700P{*}_{cr,0}$ and initial beam radius was changed from 10 cm to 180 cm. The fine continuous curves show linear propagation for each beam. The symbols in Figures (a) and (d) are reported in the parameter space shown in Fig. 3.3.

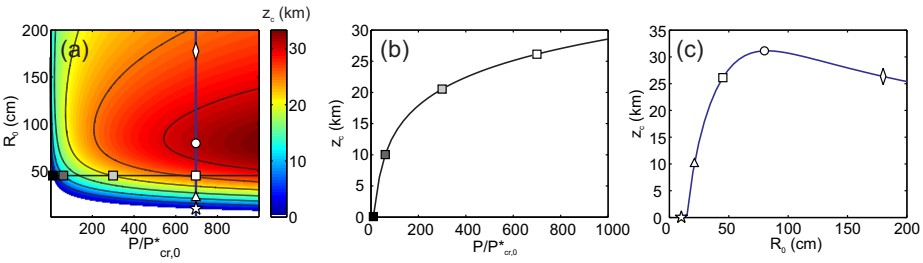

Figure 3.3: (a) Collapse distance dependence on input beam radius R_0 and power P while the beam curvature is constant $f = 390$ km. Figures (b) and (c) depict slices of parameter space depicted in (a). Figure (b) shows the collapse distance dependence on input beam power, when the initial beam radius was set to $R_0 = 45$ cm, while (c) shows the collapse distance dependence on intial beam diameter when the initial beam power was set to $P = 700P^*_{cr,0}$. Symbols depict different points in parameter space to easily identify parameters of curves shown in Fig. 3.2.

$$z_c = d\frac{A + p^{0.06}}{1 + p^{0.06}}, \tag{3.4}$$

where $d = 195$ km, $R_f = 80$ cm, $p = P/P_f$ and

$$A = -\frac{1.64 + 0.193(R_0/R_f)^3}{1 + (R_0/R_f)^3}, \tag{3.5}$$

$$\log_{10}(P_f/P^*_{cr,0}) = \frac{11.29(R_0/R_f - 0.429)^2 - 1.98}{(R_0/R_f - 0.429)^2 + 1.29}. \tag{3.6}$$

The scaling law can be used to predict the beam parameters required to initiate filamentation at desired altitude in the sky, starting from orbit. Figure 3.3 shows that filamentation from orbit can be initiated at any altitude between sea level and 35 km. However high altitudes require somewhat extreme conditions (Terawatt beam powers and meter scale beam diameters). Altitudes of a few kilometers can be targeted with beams of a few tens of centimeters carrying hundreds of Gigawatts.

Chapter 4

Direct numerical simulations of filamentation from orbit

We have numerically investigated filamentation from orbit by two different types of simulations. First, for a monochromatic pulse, the beam propagation from space to earth was performed by means of the unidirectional nonparaxial propagation equation (2.2). Second, we took into account the temporal dimension and simulated the pulse propagation as described by Eq. (2.1), accounting for full dispersion of air and spectral broadening due to self-phase modulation. In the latter case, we assumed cylindrical symmetry of the pulse around the propagation axis.

4.1 Simulations for monochromatic pulses

4.1.1 Numerical procedure

In agreement with our approximation of a time-independent electric field envelope $\mathcal{E}(x, y, z)$, we consider the electron density $\rho(x, y, z)$ as a function of intensity obtained by solving Eq. (2.5) for a pulse with maximum intensity $\mathcal{I}(x, y, z)$ and fixed Gaussian pulse shape $\exp(-2\ln 2\, t^2/T_{\mathrm{FWHM}}^2)$ with duration T_{FWHM}. This method has previously been shown to successfully capture plasma induced effects in multiple filamentation [44, 45].

We followed the spectral numerical methods thoroughly described in Ref. [38] to integrate the propagation equation (2.2). In addition, we implemented specific techniques for the propagation of large beams undergoing self focusing and collapse. From an input beam reaching the meter scale to a filament diameter of 100 μm, there is a scale ratio of 10^4. It is clearly not necessary to use the finest resolution (a grid step of $\sim 1\,\mu$m, i.e. 10^6 grid points for each transverse dimension x and y to properly discretize a filament) over the entire propagation distance from orbit to Earth since the beam is much larger over most of this length. We therefore devised procedures to start the simulation from a grid suited to the input beam width and to refine the grid via spectral techniques,

so as to double the resolution whenever it is necessary. Refining grids by spectral techniques does not introduce fitting errors. With this technique, we could propagate a 50 cm large input beam over 400 km within a few tens of minutes in (1+1)D ($\mathcal{E}(r,z)$ has radial symmetry), and a few hours in (2+1)D (no radial symmetry for $\mathcal{E}(x,y,z)$, multiple filaments can form). However, as we propagate the beam and refine resolution, we also drop the outermost grid points to keep the advantage of a reasonable number of grid points leading to a fast simulation time. There are two minor drawbacks associated with this procedure: (i) Since beam self-focusing concentrates most but not all the beam power in the center, a small amount of power contained in the beam tail is lost each time the box size is decreased. (ii) Cutting the beam tail introduces noise at the edge of the box which has to be kept under a certain threshold (five decades below the maximum amplitude) in order to prevent interaction with the rest of the beam.

4.1.2 Simulation results for monochromatic filaments

From the numerical simulations of monochromatic beam propagation performed in section 3.3, we gained valuable insight into beam dimensions and power levels needed to initiate filamentation at a desired height. The scaling law for the collapse distance (Eqs (3.4), (3.5), (3.6)) gives a quick estimation of the required powers and geometries. To describe the formation of a filament, additional plasma effects were added one after another. First plasma defocusing was considered and second nonlinear losses due to multiphoton absorption.

The results shown in Fig. 4.1 show the beam radius as a function of propagation distance, starting from orbit at $z_0 = 400$ km. The beam considerably shrinks during the focusing stage until it reaches the nonlinear focus at $\sim$ 10.015 km. Therefore, the beam evolution is plotted in four subfigures (Figs. 4.1a'–a""). Figure 4.1a"" shows the formation of the filament once plasma defocusing and multiphoton absorption regularize the collapse, and the subsequent oscillatory dynamics of the beam diameter. Figures 4.1b–c show the intensity and plasma density in the same region where the filament starts (9.98 km $< z <$ 10.03 km). Focusing-defocusing cycles are clearly visible. They reflect the competition between self-focusing and nonlinear plasma effects. When the nonlinear absorption is included, the oscillation period increases, as a fraction of the beam power is lost in each refocusing event. Note that the collapse position or the beginning of filamentation marked by the first minimum of the beam radius does not change when plasma defocusing and nonlinear losses are taken into account. This justifies our approach where only the relevant physical effects, namely, diffraction, self-focusing and the density gradient in the atmosphere were considered to predict the collapse or nonlinear focus position and determine an accurate scaling law from the beam propagation results.

4.2 Simulations for femtosecond pulses

Supercontinuum generation during filamentation can only be reproduced by numerical simulations if we relax the monochromatic approximation. We have therefore performed simulations initiated with a Gaussian pulse of 500 fs duration and a focused Gaussian beam, showing filament generation, and generation of a very broad supercontinuum at a predefined height. We first justify our

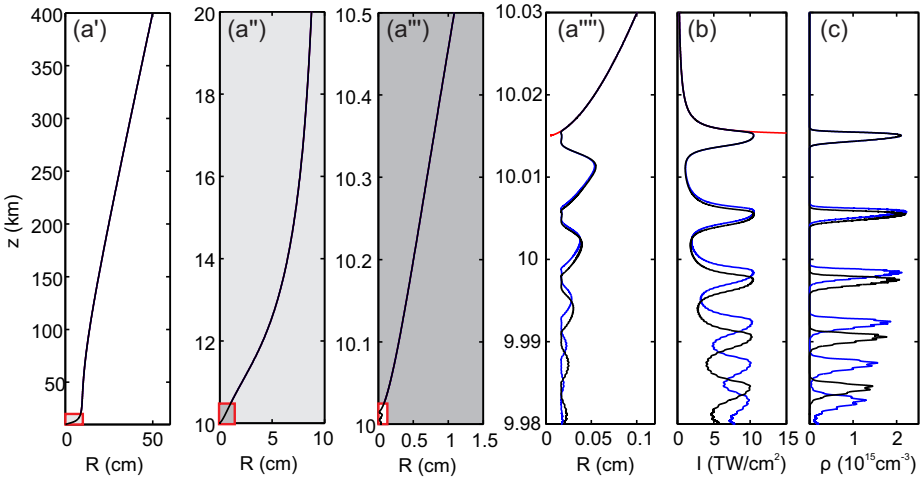

Figure 4.1: Beam width dependence on height is depicted in four graphs (a'),(a"), (a"') and (a""). Panel a' depicts beam propagation from orbit ($z_0 = 400$ km from the ground) to an altitude of 10 km from the ground. The red rectangle shows the zoomed portion of the propagation depicted in the next graphs (a"), (a"') and (a"') organized in the same way. For the filament region, the dependence of the maximum intensity and plasma density upon altitude is depicted in (b) and (c). Red curves indicate when only Kerr nonlinearity, diffraction and density gradients are included in the simulations. Blue curves: plasma defocusing is added. Black curves: plasma defocusing and nonlinear losses are added. The initial beam width was 50 cm, while the initial power was $P = 45\, P{*}_{cr} = 143$ GW.

approach to chose the pulse duration.

The collapse distances estimated in section 3.3 are valid for monochromatic pulses (narrow spectrum approximation). The pulse duration adds another degree of freedom to the determination of the collapse distance, due to group velocity dispersion during linear propagation and self-focusing. Dispersion will be more efficient for short pulses and will stretch the pulse along propagation. For instance, in air at sea level, the second order dispersion coefficient for a pulse of central wavelength of 800 nm is $k'' \sim 0.2$ fs^2/cm. This means that a 100-fs pulse will broaden by a factor of 1.4 ($\sqrt{2}$) over a propagation distance of 250 m, which is a short distance compared to the kilometric distances considered here. At an altitude of 10 km where the dispersion coefficient is about 10 times lower, the 100-fs pulse would still double its length over a few km. Consequently, dispersion tend to decrease the peak intensity and to effectively decrease the pulse power, postponing the collapse to longer propagation distances. If an initially short pulse is launched from orbit, it will undergo significant dispersion during propagation through the atmosphere. The filament and the supercontinuum will therefore be generated closer to the surface of the Earth compared to the collapse distance predicted in the monochromatic approximation.

The collapse distance is less sensitive to input pulse duration for long pulses. However, long pulses, (e.g. nanosecond pulses) introduce other challenges. Niday *et al.* have shown that intense nanosecond pulses propagating over long distances in air undergo modulational instability and pulse splitting into a sequence of shorter pulses [46]. A highly fragmented pulse is certainly not ideal for the coherence of the supercontinuum spectrum. Furthermore, for any input pulse duration, nonlinear effects lead to severe pulse shortening and pulse splitting during filamentation. The most intense portion of the pulse will compress and generate a supercontinuum, while the background intensity will remain weakly affected by nonlinearity. The most intense and shortest structures can have a duration of a few femtoseconds. Long pulses would therefore require a very large number of temporal grid points to resolve pulse splitting and supercontinuum generation accurately. This poses numerical challenges since the numerical scheme must accomodate a range of spatial and temporal scales, not only because the beam contracts from 50 cm to 100 μm, but also because a pulse of several hundreds of fs may require a temporal box of several ps with a resolution capable of describing subpulses of a few fs.

We initiated our simulations with a Gaussian pulse of 500-fs duration. This value is optimum for numerical simulations of filamentation from orbit as it ensures a trade-off between dispersion until the collapse and modulation instability during filamentation, keeping both of these effects computationally tractable with reasonable simulation times. For instance, a typical simulation over 400 km starting from orbit with a 50-cm large beam carrying the same peak power $P = 45\,P{*_{cr}}$ as in Fig. 4.1 can be completed within a week on a double Intel Xenon X5650 processor power computation machine.

Numerical simulation results are depicted in figures 4.2, 4.3 and 4.4. The input peak power $P = 45\,P{*_{cr}}$ corresponds to a 76-mJ energy for the 500-fs pulse. Propagation starts from orbit at $z_0 = 400$ km but filamentation starts at 7.312 km from the surface of the earth instead of 10 km (see Fig 4.2a) due to dispersion-induced pulse broadening. The filament radius shrinks to less than 200 μm and the high intensity (20 TW/cm^2) is sustained over $\sim$ 2 m after the nonlinear focus (Fig 4.2b). A secondary weaker intensity peak is obtained at

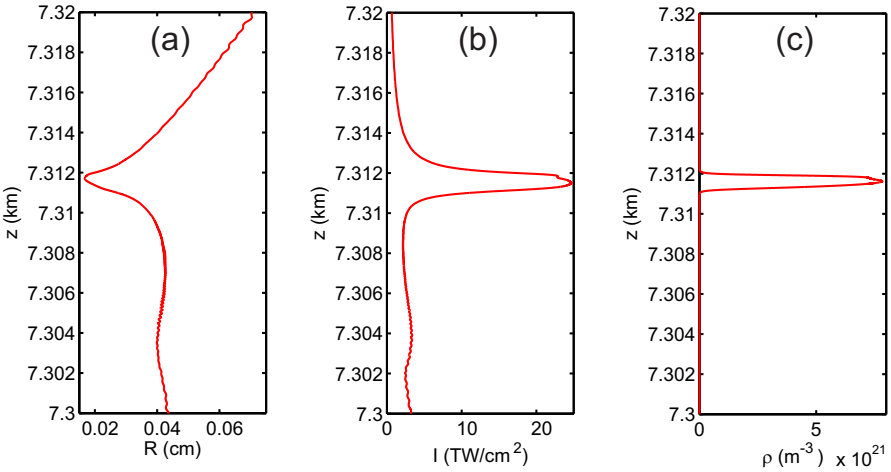

Figure 4.2: Beam width (a), intensity (b) and plasma density (c) around the nonlinear focus of the beam. Initial conditions: $z_0 = 400$ km, $\lambda_0 = 800$ nm, $R_0 = 50$ cm, $f = 390$ km, $T_{\mathrm{FWHM}} = 500$ fs, Pulse energy: 76 mJ.

7.304 km, 10 m beyond the nonlinear focus, and is attributed to beam refocusing. However, it is too weak to generate a significant plasma density (Fig 4.2c), although the beam keeps propagating in the form of an intense light tube of radius $\sim 400\,\mu$m.

Figure 4.3 shows the spectral content of the pulse undergoing filamentation at an altitude of 7.3 km, together with the spatio-temporal intensity distribution. Figure 4.3a shows standard features in the angularly resolved supercontinuum generated by femtosecond filamentation. In addition to the axial supercontinuum with high power density close to the pump wavelength ($\lambda_0 = 800$ nm) and to the propagation axis $\theta = 0$, we also recognize conical emission, a manifestation of angular dispersion, from the high intensity branches indicating that different frequencies propagate at different angles. The spectral region around these branches is populated due to scattering of the incident laser pulse off nonlinear polarization waves (the medium response) [47]. In all media with normal dispersion, this resuts in the generation of a pair of conical branches, the so-called X-waves, which constitute the skeleton of (θ–λ) spectra where a phase matching condition between the laser pulse, the nonlinear polarization wave and the scattered wave is fulfilled [48]. The integrated spectrum in Fig. 4.3c shows that the supercontinuum is smooth and spans from 300 nm to 1.1 μm. Besides the main peak at 800 nm, the spectrum shows secondary peaks at 400 and 600 nm at the intersection of the conical branches with the propagation axis ($\theta = 0$). Each of these peaks reflects the space-time dynamics of the pulse undergoing filamentation. Both peaks are actually generated by the trailing split pulse shown in Fig. 4.3d, which is responsible for the excitation of nonlinear polarization waves. The velocity of the polarization waves determines phase matching and the preferential region where the (θ–λ) spectrum is populated, which in turn determines the position of the spectral peaks in the integrated spectrum. The spatio temporal intensity distribution shown in Fig. 4.3b illustrates that

the pulse splitting phenomenon actually follows from a severe pulse reshaping involving space-time couplings.

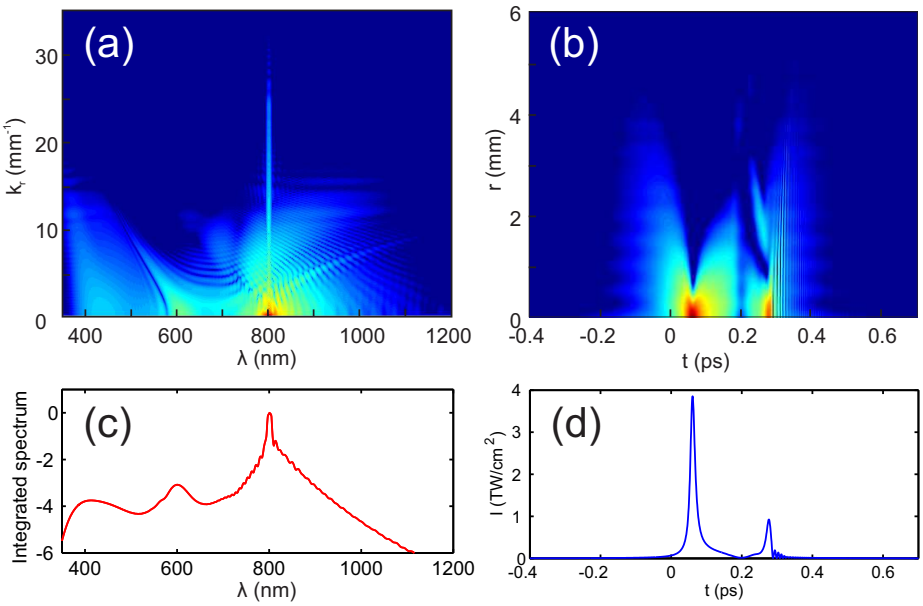

Figure 4.3: (a) Angularly resolved supercontinuum spectrum generated by filamentation, at 7.3 km from the earth, while (c) depicts the spectrum integrated over transverse wavenumbers (or angles). (b) Spatio-temporal intensity profile and (d) axial intensity profile of the pulse at $z = 7.3$ km. Initial conditions: Input beam radius $R_0 = 50$ cm, pulse duration $T_{\mathrm{FWHM}} = 500$ fs, initial beam peak power $P = 45\, P{*}_{cr} = 143$ GW and pulse energy 76 mJ.

Figure 4.4(a) shows how the integrated spectrum is populated as a function of altitude, which decreases along pulse propagation). The spectrum remains narrow until the nonlinear focus where a very quick broadening occurs. The supercontinuum reflects the formation of an intense and short pulse as displayed in Fig. 4.4b.

The fluence change with altitude shows beam focusing at 7.312-km altitude corresponding to the supercontinuum generation point. A secondary peak in the spectrum appears at 7.305-km altitude, which is connected to small refocusing of the pulse visible in Fig. 4.4 (b). The supercontinuum does not broadens to 400 nm but saturates at 600 nm due to the pulse intensity not reaching sufficiently high values. Further propagation may induce more supercontinuum generating pulses, however the numerical code was not able to propagate to the ground due to numerical noise and time restrictions.

4.3 Various species ionisation

Plasma density evaluation accounting all species dependence on altitude will increase the time needed to complete the simulations. Therefore numerical simulations were done only accounting oxygen and nitrogen molecules variation with height as the most likely species to be ionized. The retrieved intensity

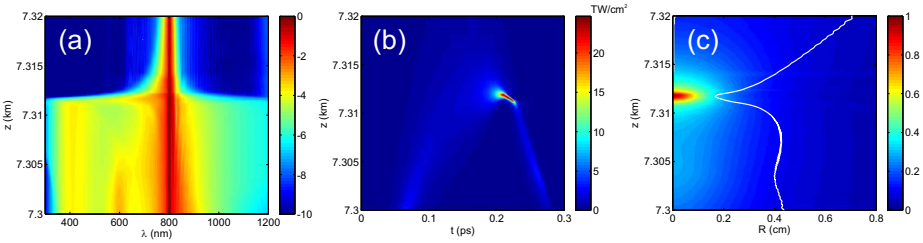

Figure 4.4: Angle-integrated spectrum (a), axial pulse profile (b) and beam fluence (c) vs altitude around the nonlinear focus of the beam. The white line in panel (c) depicts the beam radius evolution.

dependence on altitude may serve as an input for a simplified estimation of plasma densities accounting all different species depicted in Fig. 2.1. Assuming the pulse shape does not change over the whole propagation we are able to estimate ionization of different species dependence on altitude, where the pulse maximum is taken from previous numerical simulation. The easiest species to ionize is oxygen because it has lowest ionization potential. Figure 4.5 (a) shows that nevertheless the atomic oxygen is the most abundant species at very high altitudes the most of the electrons comes from ionizing oxygen. Overall the plasma density is so low that it can't affect the beam or pulse propagation. Figure 4.5 (b) shows the zoomed portion of the propagation where the filamentation started. Simulation results show that oxygen is efficiently ionized and generates dense plasma. The next abundant ionized molecule is nitrogen; however the plasma density is one order lower than ionized oxygen. The yellow curve shoes that the argon is also ionized, but the contribution to the total plasma density is four orders lower. This means that accounting argon plasma density increase in overall plasma density will not alter the nonlinear propagation of the beam. In the numerical calculations the pulse shortens to a few femtoseconds, which will even increase the differences between the different ionized species. These results show that it is possible to investigate nonlinear beam propagation accounting only oxygen and nitrogen molecules. It is interesting to note that this simplified model shows that if the pulse is very long, electrons will be efficiently accelerated and efficiently ionize most abundant species (nitrogen). Figure 4.5 (c) shows that the ionized nitrogen molecule density is higher than the ionised oxygen molecule density at the nonlinear focus.

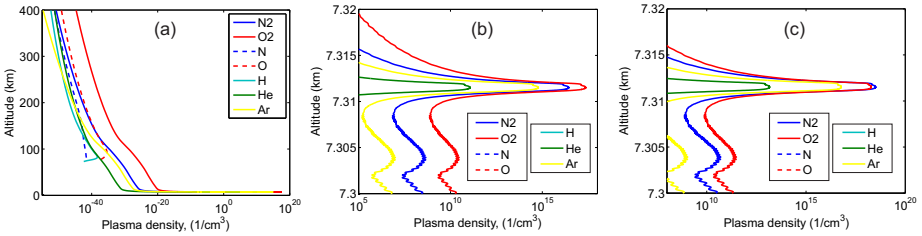

Figure 4.5: Plasma density dependence on height (a) when the pulse duration (FWHM) was fixed at 500 fs. Panel (b) shows where the filamentation starts. Panel (c) shows zoomed part of the propagation when the pulse duration (FWHM) was fixed at 5 ps.

Chapter 5

Conclusions

In this study we provided a theoretical and numerical framework for understanding spaceborne laser filamentation by modeling the optical pulse propagation starting from the nonlinear Schödinger equation. The impact of initial optical power and beam diameter was studied to estimate system requirements for laser filamentation to occur in the lower parts of the atmosphere. Our results indicate that laser filamentation from space is possible for a large range of peak pulse power, beam curvature, and beam radius. Altitudes for beam collapse ranging from 5-45 km can be reached by changing initial beam characteristics. Scaling laws for the collapse point, i.e. where filamentation is starting, were obtained based on direct simulations of nonlinear unidirectional pulse propagation equations.

Our results have shown that laser filamentation can lead to the remote generation of a supercontinuum in the atmosphere extending from 300 nm to 1.1 μm, collocated with pulse splitting and beam collapse at an altitude of 7.3 km. Propagation in the stratified atmosphere was taking into account via an air density profile depending on the molecule type and altitude profile. The atmosphere was assumed well mixed, consisting of molecular nitrogen and molecular oxygen, which are the promiment contributors to plasma generation in the atmosphere. Turbulence effects were neglected since beam sizes are much smaller than the typical scale of turbulence at altitudes where atmospheric turbulence is present.

This work was intended as a theoretical proof-of-concept of laser filamentation and remote supercontinuum generation from orbital altitudes. This work will hopefully provide a new remote sensing tool in atmospheric research: a spaceborne white-light lidar. It would enable the synoptic monitoring of various atmospheric constituents including trace gases and aerosols at various atmospheric depths from a single femtosecond laser source onboard a spacecraft, reducing the overall complexity of the system.

As a last note the self-focusing property of nonlinear laser beams can also be used for free-space optical communications. By propagating pulses just below the critical power needed for filamentation and ionisation of the atmospheric column, one can reduce the size requirements for focusing optics in space and receiving facilities on the ground [32].

Chapter 6

Next steps

As next steps, a detailed study of the possible applications of laser filamentation for spaceborne atmospheric research should be performed. Laser filamentation offers white-light lidar potential, which could be interesting for multispectral backscatter lidar applications: it could significantly improve the retrieval of aerosol size distributions and concentrations. It could also offer an atmospheric white-light source to probe different absorption bands simultaneously via multispectral differential absorption lidar. More practical considerations of the applications are sought as next steps:

This includes performing simulations of the backscattering coefficient of the white light generated in the atmosphere and its signal-to-noise ratio. This also includes having a closer look at atmospheric species and absorption bands of interest: e.g. monitoring ozone at λ =300 nm at different atmospheric depths simultaneously with other gas species such as NO_2 at λ =420 nm, BrO at λ = 350 nm or CO_2 at λ =1.5 μm and methane at 1.6 μm. A closer consideration of backscattering coefficients and wavelengths of interest would provide additional constraints on the technical requirements such as optical power levels and beam sizes. Finally the target altitude for laser filamentation should be considered more closely in view of the Earth Observation applications.

In addition a system-level studies of a spacecraft payload based on laser filamentation phenomenon is sought in the future. An analogy with the tested ground system described in [49] would require the high but technically already achievable power level of 30 kW in orbit. The ground-based system consists of a compact Ti:Sapphire oscillator and a Nd:YAG pumped Ti:Sapphire amplification chain; such systems are very sensitive to external vibrations and therefore cannot sustain launch yet. The development of coherent ultrashort pulsed fibre lasers is currently under way [50, 51] but more R&D is required to achieve space-qualification. The total weight of the tested ground system, including laser source, detection system, power supplies and heat exchanger was 10 tons. The overall ground-based system can fit in a standard sea container [49]. Since its development more than 10 years ago, notable advancements have been realized. Now the TT-Mobile laser system from Amplitude Technologies is capable of producing up to 300-mJ 40-fs pulses, consuming only 10 kW and weighting only 1.4 tons. A detailed analysis of the technical feasibility of having a similar system in orbit would be required as next steps.

Appendix A

Full theoretical model of vertical propagation of ultrashort laser pulses

A.1 Propagation equations

In this section, we derive the set of propagation equations from the wave equation in order to account for the variation of gas density with altitude. The problem of laser pulse propagation over long distances is usually described by a unidirectional propagation equation accounting for propagation phenomena in a preferential direction (forward) [38]. Neglecting backward propagating electromagnetic fields not only makes the problem computationally tractable but also corresponds to an excellent approximation for most situations of interest. For propagation in air, a significant reflexion of the pulse could occur on the plasma generated by the propagating pulse provided the plasma density reaches a critical value, $n_c = (\epsilon_0 m_e/e^2)\omega_0^2$, where ω_0 denotes the central frequency of the laser pulse. For an infrared laser pulse (800 nm), the critical plasma density $n_c = 2\times10^{21}$ cm^{-3} lies far above the density of neutral molecules at atmospheric pressure 2.5×10^{19} cm^{-3}, making negligible the reflected signal. We therefore review the assumptions in the derivation of unidirectional propagation equations and introduce air density dependence in the model.

We start from a linearly polarized laser pulse described by its electric field, the evolution of which is governed by the wave equation in a nonlinear medium:

$$\nabla^2\hat{\mathbf{E}} - \nabla(\nabla\cdot\hat{\mathbf{E}}) + \frac{n^2(\omega)\omega^2}{c^2}\hat{\mathbf{E}} = -\mu_0(\omega^2\hat{\mathbf{P}} + i\omega\hat{\mathbf{J}}) \tag{A.1}$$

Equation (A.1) is written directly in frequency space corresponding to the time variable, thus $\hat{\mathbf{E}}(\omega,\mathbf{r})$ depends on frequency ω and on three spatial coordinates. We consider the electric field as purely transverse ($\nabla\cdot\hat{\mathbf{E}} = 0$), which is a very good approximation for all situations where the laser beam is not tightly focused. This allows us to work with the scalar electric field component E along the polarization direction. On the right hand side of Eq. (A.1), $\hat{\mathbf{P}}(\omega,\mathbf{r})$ and $\hat{\mathbf{J}}(\omega,\mathbf{r})$ denote the nonlinear polarization and current which are functions of the electric

field and air density. On the left hand side, the dispersion in the medium is described by a frequency-dependent linear index of refraction $n(\omega)$ [39] and is the only quantity depending on the density of air with $n(\omega) - 1 \propto N$, where N denotes the Loschmidt's number or gas density. This dependence is however negligible as $n \simeq n_0 + \delta n_0 \times p$ where p denotes the pressure in atmosphere and $10^{-4} < \delta n_0 < 10^{-3}$. In the following, the refractive index $n(\omega)$ therefore does not depend on altitude z.

We then write $\nabla^2 = \partial_{z^2} + \nabla_\perp^2$, where z denotes the propagation direction, and factorize the propagation equation by considering that the pulse is propagating forward and neglecting the backward component. This is most easily done in the Fourier domain: $\partial_{z^2} + \nabla_\perp^2 + k^2(\omega) = \partial_{z^2} + k_z^2 \simeq 2ik_z(\omega, k_\perp)[\partial_z - ik_z(\omega, k_\perp)]$, where $k_z(\omega, k_\perp) \equiv \sqrt{k^2(\omega) - k_\perp^2}$ and $k_\perp^2 \equiv k_x^2 + k_y^2$. This leads to the unidirectional pulse propagation equation [52]

$$\partial_z \hat{\tilde{E}} = ik_z(\omega, k_\perp)\hat{\tilde{E}} + i\frac{\mu_0}{2k_z(\omega, k_\perp)}(\omega^2 \hat{\tilde{P}} + i\omega \hat{\tilde{J}}), \tag{A.2}$$

where $\hat{\tilde{E}}(\omega, k_x, k_y, z)$ as well as $\hat{\tilde{P}}(\omega, k_x, k_y, z)$ and $\hat{\tilde{J}}(\omega, k_x, k_y, z)$ depend on the frequency, transverse wavenumbers k_x, k_y and spatial coordinate z. Equation (A.2) is not formally affected by a dependence of air density with altitude. This dependence will only affect the evaluation of nonlinear polarization and current.

We will finally work with the pulse envelope $\hat{\tilde{\mathcal{E}}}(\omega, k_x, k_y, z)$ rather than with the field itself, since we consider pulses with durations of at least 30 fs (ten optical cycles at 800 nm, a standard for femtosecond lasers delivering peak powers in the terawatt range).

$$\partial_z \hat{\tilde{\mathcal{E}}} = i[\sqrt{k^2(\omega) - k_\perp^2} - k_0 - k_0'(\omega - \omega_0)]\hat{\mathcal{E}} + i\frac{\mu_0}{2k(\omega)}(\omega^2 \hat{\tilde{\mathcal{P}}} + i\omega \hat{\tilde{\mathcal{J}}}), \tag{A.3}$$

where the angular dispersion or transverse wavenumber dependence of the propagation constant in front of the nonlinear polarization has been neglected. We will also consider the monochromatic version of Eq. (2.1)

$$\partial_z \tilde{\mathcal{E}} = i[\sqrt{k_0^2 - k_\perp^2} - k_0]\tilde{\mathcal{E}} + i\frac{\mu_0}{2k_0}(\omega_0^2 \tilde{\mathcal{P}} + i\omega_0 \tilde{\mathcal{J}}), \tag{A.4}$$

where $\tilde{\mathcal{E}}(k_x, k_y, z)$, as well as $\tilde{\mathcal{P}}(k_x, k_y, z)$ and $\tilde{\mathcal{J}}(k_x, k_y, z)$ no longer depend on the frequency ω.

A.2 Medium response model

Air is a Kerr medium with a nonlinear refraction index change proportional to the beam intensity $n = n_0 + n_2\mathcal{I}$, where $n_0 \sim 1$ denotes the linear index and n_2 the nonlinear index coefficient. The optical Kerr effect is described by the nonlinear polarization,

$$\mathcal{P}(t) = 2\epsilon_0 n_0 n_2 \mathcal{I}(t)\mathcal{E}(t), \tag{A.5}$$

where $\mathcal{I} \equiv \epsilon_0 n_0 c|\mathcal{E}(t)|^2/2$ denotes the pulse intensity and the nonlinear index coefficient $n_2 \equiv 3\chi^{(3)}/4\epsilon_0 c n_0^2$ is linked to the linear refraction index n_0 and the third order nonlinear susceptibility $\chi^{(3)}$. The latter is proportional to the density

of air. The optical Kerr effect leads to beam self-focusing when the beam power $P_{\rm in}$ exceeds a threshold $P_{\rm cr} \sim 3$ GW at atmospheric pressure. This critical value corresponds to the nonlinear refraction index of air $n_2 = 3.2 \times 10^{-19}$ cm^2/W. Below, we evaluate thoroughly the conditions for self-focusing and beam collapse in the atmosphere when the density of air varies with altitude.

Once the pulse intensity is high enough, a plasma is generated by optical field ionization and by collision processes. In the atmosphere, various atomic and molecular species can liberate an electron. The main species to consider are those with the lowest ionization potential, leading to the easiest optical field ionization, and those with the higher density. We therefore model ionization processes by a set of rate equations for the density ρ_{s^+} of ions s^+ generated from single ionization of atomic or molecular species s, where s denotes any species present in the atmosphere (nitrogen N_2, oxygen O_2, etc) likely to undergo ionization.

$$\frac{\partial \rho_{s^+}}{\partial t} = W_s(\mathcal{I})\rho_s + \eta_s \rho_s \rho_e - \beta_{es}\rho_e \rho_{s^+} \tag{A.6}$$

where all densities depend on space and time, the additional relations $\rho_{s^+} = \rho_{s,0} - \rho_s$ is obtained from conservation of species and the electron density is calculated via charge conservation as $\rho_e = \sum_s \rho_{s^+}$. The background density $\rho_{s,0}$ for species s will be assumed to depend only on altitude z. The first term in Eq. (2.5) accounts for optical field ionization of species s into s^+. The second term accounts for collisional ionization with frequency $\eta_s \rho_s$. In the literature, the coefficient η_s is expressed as the product of the electron transport cross section by the averaged electron velocity [53]. Below, we link this coefficient to the collision frequency. The last term accounts for electron-ion recombination, which requires nanosecond time scales to be significant. This term can therefore be neglected with femtosecond and picosecond pulses.

In conditions small numerical apertures (NA$<$ 0.05), intense laser propagation and filamentation in air leads to tenuous plasmas. The density of electrons does not exceed 10^{17} cm^{-3}, which is sufficient to clamp the intensity below a few 10^{13} W/cm^2. In this regime optical field ionization can be described by multiphoton processes, involving $K_s \equiv \langle \frac{U_{i,s}}{\hbar\omega_0} + 1 \rangle$ photons to liberate an electron from an atom or molecule of species s, with ionization potential $U_{i,s}$, where $\langle . \rangle$ denotes the integer part. Ionization rates then read as

$$W_s(\mathcal{I}) = \sigma_{K_s} \mathcal{I}^{K_s}, \tag{A.7}$$

where the multiphoton absorption cross section σ_{K_s} can be fully determined from the Keldysh theory [30, 54, 55]. Species with the lowest ionization potential are ionized more easily, therefore molecular oxygen is expected to provide the main contribution to the plasma. Multiphoton absorption cross sections used in our calculations are provided in table 2.1

Nonlinear effects also include plasma effects on the pulse propagation (plasma absorption, plasma defocusing and multiphoton absorption) which are introduced phenomenologically in the current envelope $\mathcal{J}$. The contribution of plasma absorption and plasma defocusing is obtained classically from the Drude model, i.e., by resolving the Newton equation for an electron $d\mathbf{v}/dt + \mathbf{v}/\tau_c = -(e/m_e)\mathbf{E}$ and introducing the result into the definition of the electron current $\mathbf{j} = -e\rho_e\mathbf{v}$. We obtain $\mathbf{j} = \epsilon_0 c n_0 \sigma(1 + i\omega\tau_c)\mathbf{E}$, where σ denotes the cross section

for inverse bremsstrahlung [56]

$$\sigma = \frac{e^2}{n_0 c \epsilon_0 m_e} \times \frac{\tau_c}{1+\omega^2\tau_c^2} \tag{A.8}$$

where τ_c denotes the momentum transfer collision time. In air $\tau_c = 350$ fs at atmospheric pressure. Similar values (several hundreds of fs) are found for other gases. Since $\omega\tau_c \gg 1$, Eq. A.8 can be rewritten as $\sigma \simeq \nu_c/n_0 c\rho_{cr}$ where $\nu_c \equiv 1/\tau_c$ and $\rho_{cr} \equiv \epsilon_0 m_e \omega_0^2/e^2$ denotes the critical plasma density beyond which the plasma becomes opaque to the waves of frequency ω_0. The current envelope then reads $\mathcal{J} = \epsilon_0 c n_0 \sigma(1+i\omega\tau_c)\rho_e\mathcal{E} \simeq \epsilon_0(\nu_c + i\omega_0)(\rho_e/\rho_{cr})\mathcal{E}$. The power density dissipated by this current reads $(1/2)\mathrm{Re}(\mathbf{j}\cdot\mathbf{E}) = (1/2)\mathcal{J}\mathcal{E}^* = \sigma\rho_e\mathcal{I}$ and corresponds to the averaged energy absorbed by electrons during collisions with neutral atoms or molecules [57]. Here, collisions on different atoms or molecules contribute to the collision frequency $\sigma = \sum_s \sigma_s$. Electrons with kinetic energy exceeding the ionization potential $U_{i,s}$ of species s will in turn lead to new free electrons. Thus electrons are born from this process at the average cascade ionization rate of $\sum_s \eta_s\rho_s = \sum_s(\sigma_s/U_{i,s})\mathcal{I}$. Thus, collisional ionization rates read

$$\eta_s\rho_s \equiv \frac{\sigma_s}{U_{i,s}}\mathcal{I} \tag{A.9}$$

The contribution of multiphoton absorption to the current is obtained in a similar way: the current leads to the density of dissipated energy $\sum_s W_s(\mathcal{I})U_{i,s}\rho_s$ corresponding to optical field ionization for the different species. Therefore the total current reads

$$\mathcal{J} = \epsilon_0 n_0 c \sum_s (\sigma_s\rho_e + \frac{W_s(\mathcal{I})}{\mathcal{I}}U_{i,s}\rho_s)\mathcal{E} + i\epsilon_0\omega_0\frac{\rho_e}{\rho_c}\mathcal{E} \tag{A.10}$$

In the multiphoton ionization regime, $W_s(\mathcal{I})/\mathcal{I} \equiv \sigma_{K_s}\mathcal{I}^{K_s-1}$ where the coefficient for multiphoton absorption is linked to the coefficient in the multiphoton ionization rate $\beta_{K_s} \equiv \sigma_{K_s}K_s\hbar\omega_0\rho_s$.

A.3 State-of-the-art for beam self-focusing and collapse

In this section, we review the state of the art on self-focusing and beam collapse so as to extend the theory to account for variation of air density with the propagation distance.

The relevant parameter for self-focusing is the beam power Collapse occurs when the beam power exceeds a critical threshold $P_{\mathrm{cr}} \equiv 3.77\lambda_0^2/8\pi n_0 n_2$ (3 GW in air at $\lambda = 800$ nm) [42]. Self-focusing actually also occurs for beam powers $P_{\mathrm{cr}}/4 < P < P_{\mathrm{cr}}$ but is eventually arrested by diffraction for beams in this power range [42]. The collapse distance of a Gaussian beam with radius R_0 was determined by Marburger and coworkers [42] and reads as:

$$z_c = 0.367 z_R \left((\sqrt{\frac{P}{P_{cr}}} - m)^2 - (1-m)^2 \right)^{-1/2}, \tag{A.11}$$

where $z_R = k_0 R_0^2$ denotes the Rayleigh length and $m = 0.852$. This self-focusing stage can be shortened by linear focusing (by a lens) since the collapse distance $z_{c,f}$ obtained for a focused beam follows the lens law: $z_{c,f}^{-1} = z_c^{-1} + f^{-1}$, where z_c includes the Kerr lens effect and diffraction.

Marburger's law for collapse, i.e. Eq. (A.11), was obtained by fitting the results of numerical simulations of Gaussian beam propagation with the paraxial version of Eq. (2.2), when diffraction and the optical Kerr effect are the only effects accounted for. It is obtained by introducing Eq. (2.3), $\mathcal{J} = 0$ and a small $k_\perp/k_0$-expansion into Eq. (2.2), which is rewritten here in the space-time domain for the electric field envelope $\mathcal{E}(x, y, z)$

$$\frac{\partial \mathcal{E}}{\partial z} = \frac{i}{2k_0}\nabla_\perp^2 \mathcal{E} + i\frac{\omega_0}{c} n_2 |\mathcal{E}|^2 \mathcal{E} \tag{A.12}$$

Before performing numerical simulations in the case of self-focusing in the atmosphere with an altitude dependent nonlinear index coefficient, it is instructive to review and extend the scaling law for the position of collapse obtained analytically from eq. (A.12) for a constant n_2. The scaling is obtained by means of the moment theory [30, 42, 43], which consists in deriving and solving a set of coupled ordinary differential equations governing the evolution of moments, i.e., beam characteristics, along the propagation axis. Two moments are of interest in the case of self-focusing: the beam power $P(z) \equiv \int |\mathcal{E}|^2 d\mathbf{r}$, and squared beam width $R^2(z) \equiv P^{-1}(z) \int r^2 |\mathcal{E}|^2 d\mathbf{r}$.

Evolution equations for these moments are obtained by (i) multiplying Eq. (A.12) by $\mathcal{E}^*$, or $r^2\mathcal{E}^*$, (ii) summing with the complex conjugate of the resulting equation and (iii) integrating over spatial variables ($\mathbf{r} \equiv (x, y)$). At this stage, the resulting set of ordinary differential equations is valid for any beam shape. Evaluation of coefficients of these equations however requires an assumption on the beam shape. The averaged field envelope distribution is then modeled by a Gaussian beam $\mathcal{E} = P^{1/2}(z)\pi^{-1/2}R^{-1(z)} \exp(-r^2/2R^2) \times \exp[ib(z)r^2 + i\phi_0(z)]$, where $b(z) \equiv k_0 R'(z)/2R(z)$ denotes the beam curvature and radial symmetry has been assumed ($r^2 \equiv x^2 + y^2$). The governing equations for the beam power and radius read:

$$\frac{dP}{dz} = 0, \tag{A.13}$$

$$\frac{d^2R}{dz^2} = \frac{1}{k_0^2 R^3}\left(1 - \frac{P}{P_{cr}^*}\right), \tag{A.14}$$

where $P_{cr}^* = \lambda_0^2/2\pi n_0 n_2$. Equation (A.13) simply means that the beam power is preserved along propagation and for a constant n_2 and a beam power $P > P_{cr}^*$, Eq. (A.14) admits the solution:

$$R^2(z) = R_0^2\left[\left(1 + \frac{R_0'}{R_0}z\right)^2 - \frac{z^2}{z_c^2}\right], \tag{A.15}$$

provided that the critical power P_{cr} does not depend on the altitude z. R_0 denotes the initial beam width and R_0' is negative when the beam is focused by a lens and

$$z_c = \frac{k_0 R_0^2}{\sqrt{P/P_{cr}^* - 1}} \tag{A.16}$$

denotes the collapse distance without lens focusing ($R(z_c) = 0$ when $R'_0 = 0$). If the beam is focused by a lens of focal length f, the beam curvature is $R'_0 = -R_0/f$ and self focusing leads to collapse at the distance $z_{c,f}$ such that $R(z_{c,f}) = 0$:

$$\frac{1}{z_{c,f}} = -\frac{R'_0}{R_0} + \frac{1}{z_c} \tag{A.17}$$

which corresponds to the lens law. We note that P^*_{cr} slightly differs from its counterpart P_{cr} found by numerical fit ($P_{cr} = (3.77/4)P^*_{cr}$). Equation (A.15) also tells us that a beam focused with a focusing lens ($f > 0$) will collapse if $P > P^*_{cr}$ but a beam initially diverging ($f < 0$) will also collapse if $P > P^*_{cr}(1 + k_0 R_0^2/f^2)$. These conditions for collapse and therefore for filamentation will be modified when the nonlinear index coefficient vary with altitude.

A.4 Matrix transformation algorithm

In this numerical study a conditional resizing of the matrix was devised. The ability to alter space coordinate discretization while the beam compresses gives the ability to investigate filamentation from space. It was shown that the initial beam of 50-cm width compresses down to 100 μm. Drastic beam compression needs 10^5 number of points for accurate numerical simulations if no additional techniques are implemented. As the beam compresses the matrix will have a number of points where the intensity is equal to zero or negligible compared to the maximum beam intensity. A numerical technique was developed to remove these unwanted points while propagating the beam through atmosphere. Figure A.1 shows the technique used in this study. The matrix discretization was altered when the beam compresses twofold, leaving half of the points equal to zero. By adding additional points in between existing ones we are able to remove the zero points without loosing information about the main beam.

It can happen that the beam has very long wings due to beam reshaping. However as the beam compresses twofold the intensity at the area that we want to remove might be high enough to alter our results. Therefore additional condition had to be implemented. In this study the condition was: remove points when the beam compressed twofold if the intensity at the boarder is less than 0.01 percent of the maximum beam intensity. This way we restrict high energy loss and minimize reflections and diffraction arising because of matrix boarders.

Additional points in the matrix were added via a spectral technique that does not need interpolation procedures. The technique consists of four simple steps. First step - make the Fourier or Hankel transform to have a spectrum representation of the beam. Second step - add the same amount of zero points at the high frequency components. Third step - make the inverse Fourier or Hankel transform. Additional zeros in the spectrum does not alter the matrix width, it only adds additional points, reducing the discretization step. Fourth step - remove unwanted points and propagate the beam further in the atmosphere.

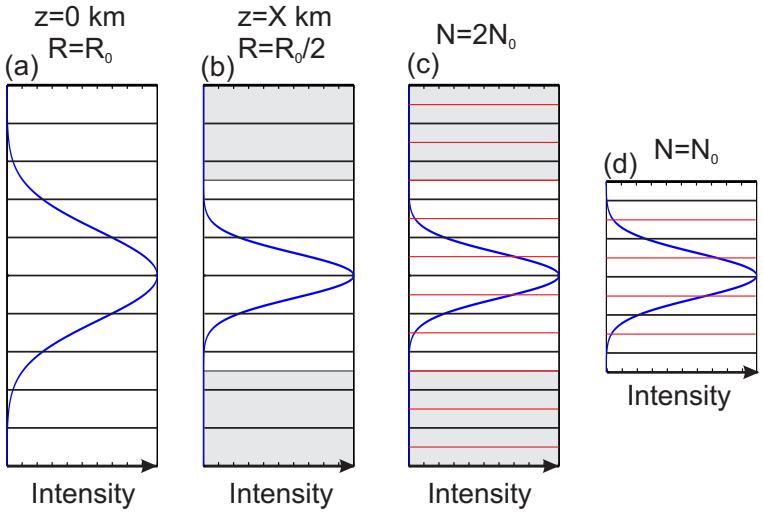

Figure A.1: Explanation of the matrix discretization change algorithm. Panel (a) represents the initial beam intensity at z=0. The Beam width is $R = R_0$. The thin lines represent discretization. Panel (b): after the beam propagates X kilometers through the atmosphere it shrinks so that the width is half its initial value. The energy contained in the light gray area is zero, i.e. the gray area is not required and such points are removed. Panels (c,d): more points are added in the beam matrix to remove the gray area, keeping the same beam but with finer discretization.

Bibliography

[1] Michael Berger, Jose Moreno, Johnny A. Johannessen, Pieternel F. Levelt, and Ramon F. Hanssen. Esa's sentinel missions in support of earth system science. *Remote Sensing of Environment*, 120(0):84 – 90, 2012. ISSN 0034-4257. The Sentinel Missions - New Opportunities for Science.

[2] CCAC State partners. Climate and clean air coalition annual report, 2014.

[3] Kirk R Smith, Michael Jerrett, H Ross Anderson, Richard T Burnett, Vicki Stone, Richard Derwent, Richard W Atkinson, Aaron Cohen, Seth B Shonkoff, Daniel Krewski, et al. Public health benefits of strategies to reduce greenhouse-gas emissions: health implications of short-lived greenhouse pollutants. *The Lancet*, 374(9707):2091–2103, 2010.

[4] David Fowler. *Ground-level ozone in the 21st century: future trends, impacts and policy implications*. Royal Society, 2008.

[5] D. S. Stevenson, F. J. Dentener, M. G. Schultz, K. Ellingsen, T. P. C. van Noije, O. Wild, G. Zeng, M. Amann, C. S. Atherton, N. Bell, D. J. Bergmann, I. Bey, T. Butler, J. Cofala, W. J. Collins, R. G. Derwent, R. M. Doherty, J. Drevet, H. J. Eskes, A. M. Fiore, M. Gauss, D. A. Hauglustaine, L. W. Horowitz, I. S. A. Isaksen, M. C. Krol, J.-F. Lamarque, M. G. Lawrence, V. Montanaro, J.-F. Müller, G. Pitari, M. J. Prather, J. A. Pyle, S. Rast, J. M. Rodriguez, M. G. Sanderson, N. H. Savage, D. T. Shindell, S. E. Strahan, K. Sudo, and S. Szopa. Multimodel ensemble simulations of present-day and near-future tropospheric ozone. *Journal of Geophysical Research: Atmospheres*, 111(D8):D08301, 2006. ISSN 2156-2202.

[6] J Lelieveld, FJ Dentener, W Peters, and MC Krol. On the role of hydroxyl radicals in the self-cleansing capacity of the troposphere. *Atmospheric Chemistry and Physics*, 4(9/10):2337–2344, 2004.

[7] Joyce E Penner, Michael J Prather, Ivar SA Isaksen, Jan S Fuglestvedt, Zbigniew Klimont, and David S Stevenson. Short-lived uncertainty? *Nature Geoscience*, 3(9):587–588, 2010.

[8] Bryan J Bloomer, Jeffrey W Stehr, Charles A Piety, Ross J Salawitch, and Russell R Dickerson. Observed relationships of ozone air pollution with temperature and emissions. *Geophysical Research Letters*, 36(9), 2009.

[9] Y Kasai, K Kita, Y Kanaya, Apollo Mission Team, et al. The japanese air pollusion observation missions, gmap-asia and apollo. In *AGU Fall Meeting Abstracts*, volume 1, page 03, 2011.

[10] Joeri Rogelj, Michiel Schaeffer, Malte Meinshausen, Drew T. Shindell, William Hare, Zbigniew Klimont, Guus J. M. Velders, Markus Amann, and Hans Joachim Schellnhuber. Disentangling the effects of co2 and short-lived climate forcer mitigation. *Proceedings of the National Academy of Sciences*, 2014.

[11] H Bovensmann, JP Burrows, M Buchwitz, J Frerick, S Noël, VV Rozanov, KV Chance, and APH Goede. Sciamachy: Mission objectives and measurement modes. *Journal of the Atmospheric Sciences*, 56(2):127–150, 1999.

[12] A Butz, S Guerlet, O Hasekamp, D Schepers, A Galli, Ilse Aben, C Frankenberg, J-M Hartmann, H Tran, A Kuze, et al. Toward accurate co2 and ch4 observations from gosat. *Geophysical Research Letters*, 38(14), 2011.

[13] Hartmut Boesch, David Baker, Brian Connor, David Crisp, and Charles Miller. Global characterization of co2 column retrievals from shortwave-infrared satellite observations of the orbiting carbon observatory-2 mission. *Remote Sensing*, 3(2):270–304, 2011.

[14] M. Buchwitz, M. Reuter, H. Bovensmann, D. Pillai, J. Heymann, O. Schneising, V. Rozanov, T. Krings, J. P. Burrows, H. Boesch, C. Gerbig, Y. Meijer, and A. Löscher. Carbon monitoring satellite (carbonsat): assessment of scattering related atmospheric co_2 and ch_4 retrieval errors and first results on implications for inferring city co_2 emissions. *Atmospheric Measurement Techniques Discussions*, 6(3):4769–4850, 2013.

[15] V. A. Velazco, M. Buchwitz, H. Bovensmann, M. Reuter, O. Schneising, J. Heymann, T. Krings, K. Gerilowski, and J. P. Burrows. Towards space based verification of co_2 emissions from strong localized sources: fossil fuel power plant emissions as seen by a carbonsat constellation. *Atmospheric Measurement Techniques*, 4(12):2809–2822, 2011.

[16] J Callies, E Corpaccioli, M Eisinger, A Hahne, and A Lefebvre. Gome-2-metop's second-generation sensor for operational ozone monitoring. *ESA bulletin*, 102:28–36, 2000.

[17] S Noël, K Bramstedt, A Rozanov, H Bovensmann, and JP Burrows. Stratospheric methane profiles from sciamachy solar occultation measurements derived with onion peeling doas. *Atmospheric Measurement Techniques Discussions*, 4(4):4801–4823, 2011.

[18] A Rozanov, S Kühl, A Doicu, C McLinden, J Puķīte, H Bovensmann, JP Burrows, T Deutschmann, M Dorf, Florence Goutail, et al. Bro vertical distributions from sciamachy limb measurements: comparison of algorithms and retrieval results. *Atmospheric Measurement Techniques*, 4(7):1319–1359, 2011.

[19] Jan Meyer, Astrid Bracher, A Rozanov, AC Schlesier, H Bovensmann, and JP Burrows. Solar occultation with sciamachy: algorithm description and first validation. *Atmospheric Chemistry and Physics*, 5(6):1589–1604, 2005.

[20] C Kiemle, M Quatrevalet, G Ehret, A Amediek, A Fix, and M Wirth. Sensitivity studies for a space-based methane lidar mission. *Atmospheric Measurement Techniques Discussions*, 4(3):3545–3592, 2011.

[21] J. Kasparian, M. Rodriguez, G. Méjean, J. Yu, E. Salmon, H. Wille, R. Bourayou, S. Frey, Y.-B. André, A. Mysyrowicz, R. Sauerbrey, J.-P., Wolf, and L. Wöste. White light filaments for atmospheric analysis. *Science*, 301:61, 2003.

[22] L. Wöste, C. Wedekind, H. Wille, P. Rairoux, B. Stein, S. Nikolov, C. Werner, S. Niedermeier, F. Ronneberger, H. Schillinger, and R. Sauerbrey. Femtosecond atmospheric lamp. *Laser und Optoelektronik*, 29(5): 51–53, 1997.

[23] M. Rodriguez, R. Bourayou, G. Méjean, J. Kasparian, J. Yu, E. Salmon, A. Scholz, B. Stecklum, J. Eislöffel, U. Laux, A. P. Hatzes, R. Sauerbrey, L. Wöste, and J.-P. Wolf. Kilometric-range nonlinear propagation of femtosecond laser pulses. *Phys. Rev. E*, 69:036607, 2004.

[24] G. Méchain, A. Couairon, Y.-B. André, C. D'Amico, M. Franco, B. Prade, S. Tzortzakis, A. Mysyrowicz, and R. Sauerbrey. Long range self-channeling of infrared laser pulses in air: a new propagation regime without ionization. *Appl. Phys. B*, 79:379–382, 2004.

[25] G. Méchain, C. D'Amico, Y.-B. André, S. Tzortzakis, M. Franco, B. Prade, A. Mysyrowicz, A. Couairon, E. Salmon, and R. Sauerbrey. Range of plasma filaments created in air by a multiterawatt femtosecond laser. *Optics Commun.*, 247:171–180, 2005.

[26] Magali Durand, Aurélien Houard, Bernard Prade, André Mysyrowicz, Anne Durécu, Bernard Moreau, Didier Fleury, Olivier Vasseur, Hartmut Borchert, Karsten Diener, Rudiger Schmitt, Francis Théberge, Marc Chateauneuf, Jean-François Daigle, and Jacques Dubois. Kilometer range filamentation. *Opt. Express*, 21(22):26836–26845, Nov 2013. doi: 10.1364/OE.21.026836. URL `http://www.opticsexpress.org/abstract.cfm?URI=oe-21-22-26836`.

[27] G. Méjean, J. Kasparian, E. Salmon, J. Yu, J.-P. Wolf, R. Bourayou, R. Sauerbrey, M. Rodriguez, L. Wöste, H. Lehmann, B. Stecklum, U. Laux, J. Eislöffel, A. Scholz, and A. P. Hatzes. Towards a supercontinuum-based infrared lidar. *Appl. Phys. B*, 77(2-3):357 – 359, 2003.

[28] G. Méjean, J. Kasparian, J. Yu, S. Frey, E. Salmon, and J.-P. Wolf. Remote detection and identification of biological aerosols using a femtosecond terawatt lidar system. *Appl. Phys. B*, 78(5):535 – 537, 2004.

[29] O. A. Bukin, M. Yu Babii, S. S. Golik, A. A. Il'in, A. M. Kabanov, A. V. Kolesnikov, Yu N. Kulchin, V. V. Lisitsa, G. G. Matvienko, V. K. Oshlakov, and K. A. Shmirko. Lidar sensing of the atmosphere with gigawatt laser pulses of femtosecond duration. *Quantum Electronics*, 44(6):563, 2014.

[30] A. Couairon and A. Mysyrowicz. Femtosecond filamentation in transparent media. *Physics reports*, 441(2):47–189, 2007. URL `http://www.sciencedirect.com/science/article/pii/S037015730700021X`.

[31] P. Sprangle, J. R. Peñano, and B. Hafizi. Propagation of intense short laser pulses in the atmosphere. *Phys. Rev. E*, 66:046418, Oct 2002.

doi: 10.1103/PhysRevE.66.046418. URL http://link.aps.org/doi/10.1103/PhysRevE.66.046418.

[32] Alexander M Rubenchik, Michail P Fedoruk, and Sergei K Turitsyn. Laser beam self-focusing in the atmosphere. *Phys. Rev. Lett.*, 102(23):233902, 2009.

[33] S Hosseini, O Kosareva, N Panov, V P Kandidov, A Azarm, J-F Daigle, A B Savel'ev, T-J Wang, and S L Chin. Femtosecond laser filament in different air pressures simulating vertical propagation up to 10 km. *Laser Physics Letters*, 9(12):868, 2012.

[34] G. Méchain, G. Méjean, R. Ackermann, P. Rohwetter, Y.-B. André, J. Kasparian, B. Prade, K. Stelmaszczyk, J. Yu, E. Salmon, W. Winn, L. A. (Vern) Schlie, A. Mysyrowicz, R. Sauerbrey, L. Wöste, and J.-P. Wolf. Propagation of fs-TW laser filaments in adverse atmospheric conditions. *Appl. Phys. B*, 80:785–789, 2005.

[35] A. Couairon, M. Franco, G. Méchain, T. Olivier, B. Prade, and A. Mysyrowicz. Femtosecond filamentation in air at low pressures: Part I: Theory and numerical simulations. *Opt. Commun.*, 259:265–273, 2006.

[36] G. Méchain, T. Olivier, M. Franco, A. Couairon, B. Prade, and A. Mysyrowicz. Femtosecond filamentation in air at low pressures: Part II: Laboratory experiments. *Optics Commun.*, 261:322–326, 2006.

[37] Riad Bourayou, Guillaume Méjean, Jérôme Kasparian, Miguel Rodriguez, Estelle Salmon, Jin Yu, Holger Lehmann, Bringfried Stecklum, Uwe Laux, Jochen Eislöffel, et al. White-light filaments for multiparameter analysis of cloud microphysics. *JOSA B*, 22(2):369–377, 2005.

[38] A. Couairon, E. Brambilla, T. Corti, D. Majus, O. de J. Ramírez-Góngora, and M. Kolesik. Practitioner's guide to laser pulse propagation models and simulation. *Eur. Phys. J. Special Topics*, 199:5–76, 2011.

[39] E. R. Peck and K. Reeder. Dispersion of air. *J. Opt. Soc. Am*, 62(8):958, 1972.

[40] J. M. Picone, A. E. Hedin, D. P. Drob, and A. C. Aikin. Nrlmsise-00 empirical model of the atmosphere: Statistical comparisons and scientific issues. *J. Geophys. Res.*, 107((A12)):1468, 2002. doi: doi:10.1029/2002JA009430.

[41] K. Labitzke, J. J. Barnett, and B. Edwards, editors. *Handbook Middle Atmosphere Program 16*. SCOSTEP, University of Illinois, Urbana, 1985.

[42] J. H. Marburger. Self-focusing: Theory. *Prog. Quant. Electr.*, 4:35–110, 1975.

[43] A. Couairon. Light bullets from femtosecond filamentation. *Eur. Phys. J. D*, 27:159–167, 2003.

[44] Guillaume Point, Yohann Brelet, Aurélien Houard, Vytautas Jukna, Carles Milián, Jérôme Carbonnel, Yi Liu, Arnaud Couairon, and André Mysyrowicz. Superfilamentation in air. *Phys. Rev. Lett.*, 112:223902, Jun 2014. doi: 10.1103/PhysRevLett.112.223902. URL http://link.aps.org/doi/10.1103/PhysRevLett.112.223902.

[45] P. Prem Kiran, Suman Bagchi, Siva Rama Krishnan, C. L. Arnold, G. Ravindra Kumar, and A. Couairon. Focal dynamics of multiple filaments: Microscopic imaging and reconstruction. *Phys. Rev. A*, 82:013805, 2010.

[46] Thomas A. Niday, Ewan M. Wright, Miroslav Kolesik, and Jerry V. Moloney. Stability and transient effects in nanosecond ultraviolet light filaments in air. *Phys. Rev. E*, 72:016618, 2005.

[47] M. Kolesik, E. M. Wright, and J. V. Moloney. Interpretation of the spectrally resolved far field of femtosecond pulses propagating in bulk nonlinear dispersive media. *Opt. Express*, 13(26):10729–10741, 2005.

[48] D. Faccio, M. Porras, A. Dubietis, F. Bragheri, A. Couairon, and P. Di Trapani. Conical emission, pulse splitting and X-wave parametric amplification in nonlinear dynamics of ultrashort light pulses. *Phys. Rev. Lett.*, 96: 193901, 2006.

[49] H Wille, Miguel Rodríguez, Jérôme Kasparian, Didier Mondelain, Jin Yu, André Mysyrowicz, Roland Sauerbrey, Jean-Pierre Wolf, and Ludger Woeste. Teramobile: A mobile femtosecond-terawatt laser and detection system. *The European Physical Journal Applied Physics*, 20(03):183–190, 2002.

[50] Sven Breitkopf, Tino Eidam, Arno Klenke, Lorenz von Grafenstein, Henning Carstens, Simon Holzberger, Ernst Fill, Thomas Schreiber, Ferenc Krausz, Andreas Tünnermann, et al. A concept for multiterawatt fibre lasers based on coherent pulse stacking in passive cavities. *Light: Science & Applications*, 3(10):e211, 2014.

[51] Joohyung Lee, Keunwoo Lee, Yoon-Soo Jang, Heesuk Jang, Seongheum Han, Sang-Hyun Lee, Kyung-In Kang, Chul-Woo Lim, Young-Jin Kim, and Seung-Woo Kim. Testing of a femtosecond pulse laser in outer space. *Scientific reports*, 4, 2014.

[52] M. Kolesik and J. V. Moloney. Nonlinear optical pulse propagation simulation: From maxwell's to unidirectional equations. *Phys. Rev. E*, 70(3): 036604, 2004.

[53] B. C. Stuart, M. D. Feit, S. Herman, A. M. Rubenchik, B. W. Shore, and M. D. Perry. Nanosecond-to-femtosecond laser-induced breakdown in dielectrics. *Phys. Rev. B*, 53(4):1749–1761, 1996.

[54] L. V. Keldysh. Ionization in the field of a strong electromagnetic wave. *Sov. Phys. JETP*, 20(5):1307–1314, 1965.

[55] F. A. Ilkov, J. E. Decker, and S. L. Chin. Ionization of atoms in the tunelling regime with experimental evidence using Hg atoms. *J. Phys. B: At. Mol. Opt. Phys.*, 25:4005–4020, 1992.

[56] E. Yablonovitch and N. Bloembergen. Avalanche ionization and the limiting diameter of filaments induced by light pulses in transparent media. *Phys. Rev. Lett.*, 29(14):907–910, 1972.

[57] C. DeMichelis. Laser induced gas breakdown:a bibliographical review. *IEEE J. Quantum Electron.*, QE-5:188–202, 1969.